An MCMC Bayesian full moment tensor inversion constrained by first-motion polarities and double couple percent

Mehrdad Pakzad[1], Mahnaz Khalili[2], Shaghayegh Vahidravesh[2]

[1]Institute of Geophysics, University of Tehran, Tehran, 1435944411, Iran

[2]Graduate Student of Geophysics, Institute of Geophysics, University of Tehran, Tehran, 1435944411, Iran

Correspondence to: Mehrdad Pakzad (pakzad@ut.ac.ir)

Abstract. Monte Carlo Markov chain (MCMC) samplings can obtain a set of samples by directed random walk, mapping the posterior probability density of the model parameters in Bayesian framework. We perform earthquake waveform inversion to retrieve focal angles or the elements of moment tensor and source location using a Bayesian MCMC method with the constraints of first-motion polarities and double couple percentage using full Green functions and data covariance matrix. The algorithm tests the compatibility with polarities and also checks the double couple percentage of every site before the time-consuming synthetic seismogram computation for every sample of moment tensor of every trial source position. Other than large earthquakes, the method is especially suitable for weak events (M < 4) that their focal mechanisms cannot be well-constrained by polarities or seismograms alone, unless a dense local network is available; something that is generally occasional. Two- and one-station solutions show more agreement with all-station solution if polarity and DC% constraints are employed. In order to examine the validity of the method, two events with the independent focal mechanism solutions are utilized. Furthermore, we also calculate data covariance matrix from pre-event noise and Green function uncertainty to obtain the errors of focal mechanisms.

1 Introduction

It should be taken into consideration that most of the time due to lack of recording or noisy content of the records in long epicentral distances, determination of the focal mechanisms of weak events are difficult. Moreover, the signal to noise ratio (SNR) for microseismic events at long periods is low, therefore, small events have to be investigated at high frequencies. Accordingly, more high frequency velocity models are required. A suite of approaches has been introduced to tackle the issues, some of which utilize a Markov chain Monte Carlo (MCMC) method in Bayesian framework.

Among other methods, two-step method of Šílený et al. (1992) consists of an iteration of a linear inversion step with fixed depth and velocity model and successive perturbation of both inside a set, bounded between two depths and two structural models. Mao et al. (1994) used their method for high frequency data up to 10 Hz. They achieved this by Green's functions calculation for an inhomogeneous medium with detailed structure. Wéber studied low-magnitude earthquakes through a series of papers. His probabilistic procedure solves the nonlinearity problem of using hypocentral location as model parameter. Routinely determined locations are usually not accurate enough in short epicentral distances where the weak events are recorded. A priori hypocenter distribution is given by observed arrival

37 times, and it is employed in a Bayesian formulation with likelihood function constructed by observed waveforms, then
38 the posterior hypocenter distribution is mapped by octree importance sampling (Lomax and Curtis, 2001). The
39 posterior probability density function (hereafter PPD) of moment tensor rate functions are sampled by a large number
40 of bootstrapped data sets with the rate functions linearly inverted using hypocenters randomly chosen from the
41 posterior hypocentral probability density function (Wéber, 2006). Stähler and Sigloch (2014) proposed a probabilistic
42 framework that samples earthquake depth, moment tensor (MT), and source time function with the neighborhood
43 algorithm. Mustać and Tkalčić (2016) used two chains approach for sampling location and MT parameters. They also
44 treated noise as a free parameter in the inversion. Ito et al. (2016) estimated the probability density functions of fault
45 parameters using MCMC method for the 2004 Sumatra–Andaman earthquake. Gu et al. (2018) applied one Markov
46 chain technique for their waveform-based Bayesian full moment tensor inversion for small earthquakes. They
47 performed source relocation, full moment tensor inversion and uncertainty analysis. In their study, Marginal-then-
48 conditional sampling of the joint distribution was first obtained for any given location and velocity model, then for
49 each sampled location and velocity model they directly sampled MT from its conditional distribution. Wéber (2018)
50 introduced a method called JOWAPO (joint waveform and polarity) inversion. The method constructs a posterior
51 probability density of strike, dip and rake and maps it by octree importance sampling. The PPD consists of a null a
52 priori information and two likelihood functions for polarities and waveforms. For the details about the polarity
53 likelihood refer to Brillinger, 1980; Walsh et al. 2009 and Wéber 2018. Comparing to waveform data, the information
54 content of first-motion polarities of body waves is low, that is why a dense coverage of focal sphere is required for a
55 reliable result. On the other hand, for high frequency weak events, available velocity distributions are usually not
56 detailed enough to model their waveforms and retrieve the focal mechanisms, that is, waveforms can be modelled
57 convincingly just for relatively close stations to receive a quite dependable focal mechanisms solution for near station
58 earthquakes. However, seismic networks are not usually dense enough to make sufficient data available for inversion.
59 Therefore, combining polarity data with near-station records can be helpful. In the case of a small event occurrence
60 and with low number of stations, the objective cannot be more than to retrieve its DC focal mechanism with the
61 uncertainty. Earthquakes source inversion is relevant to the location determination and also velocity models.
62 Uncertainty in both the model parameters (here DC mechanisms), first motion observations and seismic waveform
63 should be merged by an inversion technique. In this regard, the most suitable inversion method is Bayesian sampling
64 producing an ensemble of DC focal mechanisms based on the posterior probability distribution. (Wéber, 2018).
65 As to the constraints, various methods adopted them for retrieving focal mechanisms of weak events in sparse
66 networks. For example, the phase and waveform amplitude can be combined with the first-motion P polarities and
67 average S/P amplitude ratios (Li et al., 2011). The focal mechanisms obtained by a broad set of the first-motion
68 polarities can be constrained by a single-station waveform inversion (Fojtíková and Zahradník, 2014). In this study
69 we perform waveform inversion but constrain it by first motion polarities and DC% for tectonic earthquakes. The
70 method can work with strike, dip and rake and also for the elements of MT as the model parameters; therfor for non-
71 tectonic earthquakes, DC% constrain can be eliminated. Here we describe full moment tensor and location inversion.
72 In the following sections, after a brief introductory overview of the intended methods used in this study, the performed
73 synthetic tests are described. It is preceded with the testing the method on two earthquakes in Switzerland and Iran.

74

2 Method

76

77   The PPD is computed using the Bayesian rule to the parameters $\boldsymbol{m}$, that can be strike, dip and rake or elements of MT

78   and $\boldsymbol{x}$, the location; given polarities, $\boldsymbol{P}$ and waveforms, $\boldsymbol{d}$

79

80    $\sigma(\boldsymbol{m}, \boldsymbol{x}|\boldsymbol{P}, \boldsymbol{d}) \propto \rho(\boldsymbol{x})\,\rho(\boldsymbol{m})\,L_P(\boldsymbol{P}|\boldsymbol{m}, \boldsymbol{x})\,L_d(\boldsymbol{d}|\boldsymbol{m}, \boldsymbol{x}),$ (1)

81

82   where, $\rho(\boldsymbol{x})$ and $\rho(\boldsymbol{m})$ are the prior information about $\boldsymbol{x}$ and $\boldsymbol{m}$; $L_P(\boldsymbol{P}|\boldsymbol{m}, \boldsymbol{x})$ and $L_d(\boldsymbol{d}|\boldsymbol{m}, \boldsymbol{x})$ are the likelihood

83   functions for polarities and waveforms. The uniform distribution assumptions are considered for both of the prior

84   probability densities, that is, all trial locations have equal chance before considering data and the boundary values of

85   the coefficients of elementary seismograms are set to -1.5 and 1.5. Unlike Wéber (2018), we only benefit from the

86   reliable polarities as constraints for the inversion, therefore we consider $L_P(\boldsymbol{P}|\boldsymbol{m}, \boldsymbol{x})$ to be equal to one. The Gaussian

87   model waveform likelihood is given by

88

89    $L_d(\boldsymbol{d}|\boldsymbol{m}, \boldsymbol{x}) \propto \exp[-\frac{1}{2}\,(\mathbf{G}(\boldsymbol{x})\boldsymbol{m} - \boldsymbol{d})^T\,\mathbf{C}_D^{-1}\,(\mathbf{G}(\boldsymbol{x})\boldsymbol{m} - \boldsymbol{d})],$ (2)

90

91   where $\mathbf{G}(\boldsymbol{x})$ is the spatial derivative of the Green's function at the source location $\boldsymbol{x}$ and $\mathbf{C}_D = \mathbf{C}_d + \mathbf{C}_T$, that is,

92   waveform uncertainties and theoretical uncertainties combined by adding the respective covariance operators to obtain

93   the total covariance matrix (Tarantola, 1987).

94   The inverse problem is linear in $\boldsymbol{m}$ and nonlinear in $\boldsymbol{x}$, which results in complex structure of the joint posterior

95   distribution of the model parameters. In their waveform-based Bayesian full moment tensor inversion, Gu et al. (2018)

96   designed an MCMC approach to incorporate variation in $\boldsymbol{x}$ into the problem. They first obtain the marginal posterior

97   probability distribution $\sigma(\boldsymbol{x}^*|\boldsymbol{d})$ for any given $\boldsymbol{x}$ and use it to calculate the Metropolis acceptance ratio. The adaptive

98   Metropolis method of Haario et al. (2001) is used to draw a new proposal model $\boldsymbol{x}$. Then for each sampled $\boldsymbol{x}$, they

99   directly sample $\boldsymbol{m}$ from its analytical covariance matrix. The algorithm is called marginal-then-conditional sampling

100   (Fox & Norton, 2015) that only needs one Markov chain to explore the posterior probability density. Employing

101   polarities in the inversion also makes finding $\boldsymbol{m}$ nonlinear. We implement two chains for sampling location and MT

102   parameters. The second chain to sample MT is inside the first one which samples location. The procedure to sample

103   $\boldsymbol{x}$ in the first chain is the same as used in Gu et al. (2018), that is a metropolis test which is used to determine whether

104   to accept or reject a trial $\boldsymbol{x}$ according to marginal posterior distribution for any sampled $\boldsymbol{x}$ without reference to the

105   values of MT; but for the inner sampling of $\boldsymbol{m}$, we explore $L_d(\boldsymbol{d}|\boldsymbol{m}, \boldsymbol{x}^*)$ in Eq. (2) by Metropolis-Gibbs sampler

106   described by Lomax et al. (2000). They employ Metropolis-Gibbs Sampling algorithm for probabilistic earthquake

107   location in 3D space (NonLinLoc program), here we use it in 6D space to retrieve MT. The procedure explores the

108   PPD by directed walk towards high likelihood regions. The new walk site $\boldsymbol{m}_{new}$ is obtained from the current site

109   $\boldsymbol{m}_{curr}$, by adding a vector of arbitrary direction $d\boldsymbol{m}$, with length l. The new site is accepted, if $\sigma(\boldsymbol{m}_{new}, \boldsymbol{x}^*|\boldsymbol{d}) \geq$

110   $\sigma(\boldsymbol{m}_{curr}, \boldsymbol{x}^*|\boldsymbol{d})$, otherwise the new site is accepted with probability $\sigma(\boldsymbol{m}_{new}, \boldsymbol{x}^*|\boldsymbol{d})\,/\,\sigma(\boldsymbol{m}_{curr}, \boldsymbol{x}^*|\boldsymbol{d})$. In order to

111 achieve a good coverage of PPD, determination of the step size l is essential. The algorithm does this adaptively in

112 stages. In the first stage called the learning stage, the step size is constant and relatively large enough to explore all

113 the solution space and to wander towards high likelihood regions. In the equilibration stage, the searching of high

114 likelihood regions can continue or these regions may begin to be searched for the optimum point. To achieve that, l is

115 set equal to $f_s(S_{m1}S_{m2}S_{m3}S_{m4}S_{m5}S_{m6}/N_s)^{1/6}$, where $f_s = 16$ is the scaling factor and S stands for standard

116 deviation. N_s is the number of samples to be accepted during the saving stage. In the final saving stage the step size is

117 fixed at its final value from the previous stage and the walk can continue to explore high likelihood regions (Lomax

118 et al., 2000). The polarity constraint and arbitrary DC% condition for tectonic earthquakes are applied inside the

119 second chain, that is, after sampling MT, the polarity and DC% tests are performed for compliance and if the conditions

120 are fulfilled, then the metropolis test is performed, otherwise the sample is rejected.

121 We employ Vackář et al. (2017) method for calculating $\mathbf{C}_d$. Data covariance matrix is constructed from pre-event

122 noise which allows an automated weighting of the records according to their SNR. In other words, it plays the role of

123 automated frequency filter containing noisy frequency ranges in the frequency domain. The noise generation is

124 supposed to be a random Gaussian stationary process. Therefore, with additional ergodicity assumption taken into

125 account, the covariance function is estimated from a time series autocorrelation. This matrix can be assigned to one

126 station by calculating the covariance function from the cross correlations of three components. This way, each station

127 have nine matrix blocks. It can also be assumed that noises at distant stations for high frequencies are not correlated,

128 so that the off-diagonal blocks in the main covariance matrix have zero values. The other source of error is theoretical.

129 Green function uncertainty is mostly related to the random time shifts of the data, accordingly this feature can be

130 employed to obtain approximate covariance matrix for $\mathbf{C}_T$ (Hallo and Gallovič, 2016; Hallo et al., 2017). $\mathbf{C}_d$ takes

131 precedence for weaker earthquakes (with significant uncorrelated noise) that is while $\mathbf{C}_T$ is dominant for stronger

132 (uncorrelated noise free) earthquakes. In the following we apply the method to two earthquakes with M$_W$ 3.7 and 3.8;

133 for both, $\mathbf{C}_d$ is dominant.

134 The computational cost of running the code on a 2.60 GHz Dual-Core CPU, 4G memory PC, for 1000 iterations in

135 location chain and 10^5 iterations in MT chain, is less than a minute to a few minutes for each γ explained in the

136 synthetic test section below. The speed conversely depends on the number of station/components and is proportional

137 to the number of restrictive polarities. For example, in one of the applications below with 24 seismogram components,

138 14 polarities, 9261 potential sources, and the starting point at the farthest corner of the location grid, the time is about

139 3.5 minutes. Without the constraints the time may increase even to hours.

140

141 **3 Synthetic test**

142

143 We perform several synthetic tests to confirm the validity of the method. The configuration of the stations in the

144 synthetic tests is identical to the recording stations of Sargans earthquakes used also as an application (Fig. 1).

145 The elements of MT in NED coordinate system used are as follows: m_{xx} = -2.7645e+16, m_{yy} = 3.2959e+15, m_{zz} =

146 2.4349e+16, m_{xy} = 1.1381e+18, m_{xz} = 1.8408e+17, m_{yz} = 3.6964e+17, with about 86%, 14% and 0%, DC, CLVD

147 and isotropic components. The strike, dip and rake are equal to 89.05º, 72.74º and 171.82º successively. The synthetic

148   location is located at $\boldsymbol{x}$ = (1 km N, -1 km E, 6 km down) with respect to Sargans earthquake epicenter. We used 9261

149   trial sources with equal step of 1 km from -10 to 10 km for horizontal coordinates and between 1 and 21 km for depth.

150   The results with different Signal-to-noise ratio (SNR) are shown in Table 1-3. SNR is here defined as the power of

151   signal divided by the power of white noise. A Butterworth filter with the frequency range 0.02 - 0.15 Hz is applied to

152   both the noise and synthetic data. The inversion is performed with the same velocity model as used to produce the

153   synthetic data. In the tables, beachballs of the solutions (in red) are illustrated with the true mechanism used for

154   creating synthetic seismograms in green color. Kagan angles (Kagan, 1991) are the angles of rotation between two

155   nodal planes of the solutions and the true mechanism. In Table 1 we utilize all stations in the inversion while in Tables

156   2 and 3 we just used two nearby stations, LIENZ and SGT04. Table 2 and 3 differ in using the constraints of polarity

157   and DC% > 70 in Table 2. The results presented in Table 1 and Table 2 are more close to each other; although in the

158   latter, we just used two stations. On the other hand, the results in Table 3 shows that the solutions deteriorate more, in

159   terms of Kagan angles and deviatoric part due to the lack of polarity and DC% constraints. For example, for SNR

160   equal to 0.5, Kagan angle is 8⁰, in case of applying the constraints, while it increases to 30⁰ otherwise. For the case of

161   using all stations, we calculate the location as model parameter (Table 1) while for two-station cases we fix the location

162   to the one obtained for all-station computation (Table 2 and 3).

163   The outer chain consists of drawing samples by the adaptive Metropolis method and calculating the marginal posterior

164   probability for any given location and performing the acceptance test which is a Metropolis test. The iteration is

165   repeated for 1000 times, however after few hundred steps, the optimum location is found. In the synthetic test without

166   noise, 38 iterations were enough for location parameters to converge. Similar to Mustać and Tkalčić (2016) the visited

167   potential locations, as well as the accepted location solution with the increasing likelihood and the optimum one are

168   shown in Fig. 2. Both the 3D and 2D views are illustrated. The starting search point is $\boldsymbol{x}$ = (0, 0, 10) representing the

169   beginning of the lines connecting the accepted solutions; finally ending with the maximum a posteriori solution

170   encircled by green squares in 2D views. In 3D view, the accepted Metropolis locations are drawn by green cubes. As

171   is presented in the figure, the concentration of high probability sites (larger cubes and squares) are around the optimum

172   solution, and the accepted solutions find their ways around it.

173   We applied the posterior coarsening method introduced by Miller and Dunson (2015) to reduce the sensitivity of $\boldsymbol{x}$ to

174   noise. If the dataset is large, the marginal likelihood value changes substantially for small variations of $\boldsymbol{x}$. A coarsened

175   marginal posterior probability distribution can remedy the problem, which is raising the marginal likelihood to the

176   power of $1/\gamma$ with $\gamma > 1$ (Eq. (3)).

177

178    $$\sigma_\gamma(d|x) \coloneqq (\sigma(d|x))^{1/\gamma} \tag{3}$$

179

180    $\sigma_\gamma(d|x)$ is more flat for larger γ and data cannot constrain source location, on the other hand, for small γ , $\sigma_\gamma(d|x)$

181   causes the posterior on $\boldsymbol{x}$ to be limited to a few values. The former causes the marginal posterior distribution of $\boldsymbol{x}$ to

182   degenerate to the prior, and the latter situation is susceptible to noise (Gu et al., 2018). That is why the adjustment of

183   γ is necessary, especially for obtaining optimum depth; the horizontal source coordinates are less sensitive to the

184   noise. For investigating source location variation, we plot the mean of MCMC trace versus γ (Fig. 3). The calculations

185   are performed for two cases, one in which starting point is near to the synthetic data source location (Fig.3, left panel)
186   and the other with starting point in the place of the farthest location node of the $20 \times 20 \times 20$ km grid (Fig. 3, right
187   panel). For both of the cases, SNR is 2. In the former situation the mean equals to the input location for all values of
188   low γ. Epecially for horizontal coordinates of the location; the means do not change for γ up to 300, while the depth
189   is more sensitive to the value. In the latter condition we have much longer burn-in period that are discarded before
190   plotting. The source location lastly reaches the correct input location, but there is a value of γ below which the range
191   begin to shrink and the curves of source location range versus γ show trends. This value can be chosen as the optimum
192   values of γ shown by the black circles. For this case this optimum value is 50. The figures also illustrate the standard
193   deviations by gray shaded error bars (Campbell, 2009) which show the increment for larger γs. That is due to more
194   flat $\sigma_\gamma(d|x)$ and failure of data to constrain x that is visible in the plot of vertical coordinate of the location, but
195   happens also for horizontal coordinates for higher γs than 300 (not shown in the figures).
196   Figure 4 shows the random walk in the focal angles' solution space utilizing all stations with no usage of noise (first
197   row in Table 1). The strikes, dips and rakes are calculated from the actual random walk in MT space. For simplicity
198   we only show the search in focal angles' space. The unvisited sites are shown by gray color and low and high
199   probability areas are depicted by a range of hot pallet colors from white to black. The start and end of the overall
200   search are illustrated by the green arrow and circle, respectively. The green lines show the path of all accepted focal
201   angles for all accepted locations. The total number of tested sites are 10^5, however in the figure we only demonstrate
202   the proposed and accepted sites which pass through the test of polarity and DC% in terms of the value of PPD. The
203   accepted focal angles and the relevant path for all accepted trial locations are shown by green circles and lines. There
204   are six accepted locations with the increasing likelihood out of 1000 tested locations.

4 Application

207   We present the results of applying the method on two small (M_w 3.6 and 3.8) events with available independent focal
208   mechanism solutions. The first earthquake, which was also used in the synthetic tests above, is a Switzerland event
209   near Lichtenstein border. The second one is an Iranian event happened near the capital, Tehran, called Malard
210   earthquake.

4.1 Sargans Earthquake

213   The first earthquake is an M_W 3.6 earthquake at Sargans, Switzerland which happened on December 27, 2013 at
214   07:08:28 UTC. Figure 1 shows the reference DC solution retrieved by Bayesian ISOLA (Vackář et al., 2017) with the
215   mechanism, strike, dip and rake equal to 91/183, 78/79 and 169/12. We use 14 first-motion polarities to constrain the
216   solution resulted from broadband station inversion including the polarities of four other stations: GEA0, INS7, TMO20
217   and TMO22, not shown on Fig. 1 due to their larger epicentral distances comparing to the other illustrated stations.
218   Firstly, we test the method using all stations and all polarities. We filtered the records in frequency range 0.02 to 0.15
219   Hz by Butterworth filter and inverted in the displacement domain. The results are presented in Fig. 5 to 10 and Table
220   4. Figure 5 shows the tested locations for 1000 iterations.

221   The selected γ for Sargans earthquake is 35 (Fig. 6). Actually, there is a range of values that gives identical location

222   solution beginning from $\gamma = 1$. Sargans earthquake does not show the shrinkage part even with the starting point in

223   the left top most corner of the location grid, that is, away from the optimum source location. Again the calculations is

224   performed after discarding the burn-in samples and the full source location range is the box with vertices x = (-10, -

225   10, 1) and x = (10, 10, 21), with 9261 trial source positions.

226   Figure 7 is an illustration of the inner chain searching for optimum MT for any accepted solution. From among 10^5

227   tested moment tensors for each given location only 638 sites go through the CPU intensive synthetic seismograms

228   calculations due to polarity and DC% test. For example, for the last and optimum source location, there are 149 MT

229   sites in this event.

230   As an example, all visited focal angles and accepted solutions with higher likelihood for LIENZ and SGT04 stations

231   inversion are shown in Fig. 8. In two-station calculations, the location is fixed to the estimated value of all-station

232   result, therefore Fig. 8 contains less visited sites.

233   The DC solution of Sargans earthquake is a strike-slip mechanism. It is obtained for full $\mathbf{C}_D$, that is, considering both

234   data and theoretical uncertainties and in the displacement domain (Fig. 9). For this event data uncertainty is dominant

235   over the Green function uncertainty. The waveform comparisons are illustrated for standardized data, that is, original

236   waveforms multiplied by Cholesky decomposition of the $\mathbf{C}_D$ (Fig. 10). Covariance matrix plays the role of automatic

237   frequency filter reducing the effect of noisy part of the spectrum, thus improving the result (Vackář, et al., 2017).

238   Variance reductions is 0.82 and strike, dip and rake are, 88/180, 80/80 and 170/10 with the magnitude of M_w 3.6. That

239   is in comparison with inverting without covariance matrix or with the diagonal one whose elements are chosen to be

240   the mean squared value of the waveforms with calculated variance reduction of 0.57. The event is a shallow earthquake

241   with estimated 6 km hypocentral depth and horizontal shift of 0.5 and 1 km to the north and west of the epicenter.

242   Table 4 contains the result of the inversion for two- and one-station. Only two nearby stations are used and both of

243   the solutions with and without the constraints of polarity and DC% are determined. The first row of the table contains

244   the result of the inversion using all stations (red nodal lines) with the solution of Bayesian ISOLA also depicted in

245   green. Kagan angle in the first row is the comparison made with Bayesian ISOLA solution, but other angles are

246   determined in comparison with our own all-station solution. Although the two-station no-constraints DC solutions are

247   better in terms of Kagan angle but deviatoric solutions deteriorate. One-station results become worse both in regard

248   to Kagan angle and deviatoric part of the MT. Overall, as is the case with synthetic tests, polarity and DC% constraint

249   can help to obtain better results when using lower number of stations.

250

4.2 Malard earthquake

252   Here we apply the method on the second event happened around the town of Malard near Tehran, Iran, with M_W 3.8,

253   on December 26, 2017 at 21:24:34 UTC (Fig 11). The reference solution of this event is our solution, that is, the

254   result of inversion by ISOLA (Zahradník, and Sokos, 2019) utilizing all shown stations that resulted in strike, dip and

255   rake equal to 24/118, 56/83 and -7/-145.

256   Figure 12 shows the plot of source location versus γ for Malard earthquake. The chosen γ is 10 and the source location

257   found is x = (-1, 4, 12), which is near to the location found by ISOLA using all stations, that is x = (-3, 3, 11.8). The

258   north-east horizontal location have a small shrinkage part, while it does not exist for east-west location. The shrinking
259   stage is longer for the vertical component of the location. The lack of shrinking stage for Sargans earthquake and it
260   existence for Malard event could be due to higher level of noise in case of Malard event and the low number of station-
261   components used for its calculation.

262   In order to apply the method on this earthquake, we utilize 21 first-motion polarities from broadband and short-period
263   records. The observed seismograms of HSB, VRN, JIR1, FIR and QSDN stations are filtered to frequency ranges
264   0.04-0.17, 0.04-0.08, 0.055-0.085, 0.055-0.085 and 0.055-0.08 to gain better waveform fit (Variance reduction =
265   0.79). The resulted strike, dip and rake are 26/119, 58/84 and -7/-148 (Fig 13).

266   We also determine two- and one-station solutions for this event. The results for this event show the advantage of the
267   constraints of polarity and DC% again. Of course, for all the cases, only one polarity is enough to constrain the solution
268   to the optimum solution. That is except in the case of using the single station of VRN, in which more polarity
269   constraints are needed for better compatibility with all station solution.

270

271   **5 Conclusion**

272   We employed Bayesian framework using an MCMC algorithm to retrieve full moment tensor and source location of
273   earthquakes by applying the constraints of polarity and DC%. The results show that the constraints can help to obtain
274   better results in case of restricting the number of broadband stations to two or one. This is helpful, for example, when
275   many short-period stations and therefore many polarities are available but the broadband network is sparse. The
276   obtained results indicate that despite the low magnitude of the selected earthquakes, the employed approach could be
277   reliable for retrieving location and moment tensors. The study added some methodical insights to the broad suite of
278   similar methods including the two chain approach used comprising Metropolis-Gibbs Sampling algorithm and the
279   coarsened likelihood for the parameter of source location.

280

281   **Data availability**

282   The data used in this study are freely available from Switzerland (Swiss Seismological Service (SED) at ETH Zürich
283   1983), ZAMG (Vienna), International Institute of Earthquake Engineering and Seismology (IIEES) and Iranian
284   Seismological Center (IRSC) of Institute of Geophysics, University of Tehran.

285

286   **Author contribution**

287   M. Pakzad developed the code, did the synthetic tests and prepared the manuscript. M. Khalili performed the
288   calculations of Sargans earthquake and helped making the figures. Sh. Vahidravesh performed the calculations of the
289   Malard earthquake and helped making the figures.

290

291   **Acknowledgments**

292   Data used in the study is from Switzerland (Swiss Seismological Service (SED) at ETH Zürich 1983), ZAMG
293   (Vienna), International Institute of Earthquake Engineering and Seismology (IIEES) and Iranian Seismological Center
294   (IRSC) of Institute of Geophysics, University of Tehran.

295

References

296

Brillinger, D.R., Udias, A. and Bolt, B.A.: A probability model for regional focal mechanism solutions, B SEISMOL SOC AM. 70 (1): 149–170, 1980.

Fojtíková, L. and Zahradník, J.: A new strategy for weak events in sparse networks: The first-motion polarity solutions constrained by single-station waveform inversion, SEISMOL RES LETT: 85(6), 1265-1274. https://doi.org/10.1785/0220140072, 2014.

Fox, C. & Norton, R.A.: Fast sampling in a linear-Gaussian inverse problem, SIAM/ASA J. Uncertainty. Quantification, 4, 1192–1218. https://doi.org/10.1137/15M1029527, 2015.

Gu, C., Marzouk, Y.M. and Toksöz, M.N.: Waveform-based Bayesian full moment tensor inversion and uncertainty determination for the induced seismicity in an oil/gas field, GEOPHYS J INT, 212(3), 1963-1985. https://doi.org/10.1093/gji/ggx517, 2018.

Hallo, M. and Gallovič, F.: Fast and cheap approximation of Green function uncertainty for waveform-based earthquake source inversions, GEOPHYS J INT, 207(2), 1012-1029. https://doi-org.eres.qnl.qa/10.1093/gji/ggw320, 2016.

Hallo, M., Asano, K. and Gallovič, F.: Bayesian inference and interpretation of centroid moment tensors of the 2016 Kumamoto earthquake sequence, Kyushu, Japan, EARTH PLANETS SPACE, 69(1), p.134. https://doi.org/10.1186/s40623-017-0721-4, 2017.

Haario, H., Saksman, E. & Tamminen, J.: An adaptive metropolis algorithm, BERNOULLI, 7, 223–242. https://doi.org/10.2307/3318737, 2001.

Ito, T., Gunawan, E., Kimata, F., Tabei, T., Meilano, I., Agustan, Ohta, Y., Ismail, N., Nurdin, I., Sugiyanto, D.: Co-seismic offsets due to two earthquakes (Mw 6.1) along the Sumatran fault system derived from GNSS measurements, EARTH PLANETS SPACE 68, 57, http://dx.doi.org/10.1186/s40623-016-0427-z, 2016.

Kagan, Y.Y.: 3-D rotation of double-couple earthquake sources, GEOPHYS J INT, 106(3), 709-716, https://doi.org/10.1111/j.1365-246X.1991.tb06343.x, 1991.

Campbell, R., 2009: Shaded error bars (https://github.com/raacampbell/shadedErrorBar), MATLAB Central File Exchange, last access: 1 October 1, 2019.

322

Li, J., Zhang, H., Sadi Kuleli, H. and Nafi Toksoz, M.: Focal mechanism determination using high-frequency waveform matching and its application to small magnitude induced earthquakes, GEOPHYS J INT, 184(3), 1261-1274, https://doi.org/10.1111/j.1365-246X.2010.04903.x, 2011.

Lomax, A. and Curtis, A.: Fast, probabilistic earthquake location in 3D models using oct-tree importance sampling. In Geophys. Res. Abstr, Vol. 3, 955, 2001.

Lomax, A., Virieux, J., Volant, P. and Berge-Thierry, C.: Probabilistic earthquake location in 3D and layered models. In Advances in seismic event location, 101-134, SPRINGER, Dordrecht, https://doi.org/10.1007/978-94-015-9536-0_5, 2000.

Mao, W.J., Panza, G.F. & Suhadolc, P.: Linearized waveform inversion of local and near-regional events for source mechanism and rupturing processes, GEOPHYS J INT, 116, 784–798, https://doi.org/10.1111/j.1365-246X.1994.tb03296.x, 1994.

Miller, J.W. and Dunson, D.B.: Robust Bayesian inference via coarsening, J AM STAT ASSOC, 1-13, https://doi.org/10.1080/01621459.2018.1469995, 2018.

336 Mustać, M. & Tkalčić, H.: Point source moment tensor inversion through a Bayesian hierarchical model, GEOPHYS
337 J INT, 204(1), 311–323, https://doi.org/10.1093/gji/ggv458, 2016.

338 Šílený, J., Panza, G.F. & Campus, P.: Waveform inversion for point source moment tensor retrieval with variable
339 hypocentral depth and structural model, GEOPHYS J INT, 109, 259–274, https://doi.org/10.1111/j.1365-
340 246X.1992.tb00097.x, 1992.

341 Stähler, S. and Sigloch, K.: Fully probabilistic seismic source inversion-Part 1: Efficient parameterization, SOLID
342 EARTH, (2), 1055-1069, https://doi.org/10.5194/se-5-1055-2014, 2014, 2014.

343 Swiss Seismological Service (SED) at ETH Zürich: National Seismic Networks of Switzerland; ETH Zürich,
344 https://doi.org/10.12686/sed/networks/ch, 1983.

345 Vackář, J., Gallovič, F., Burjánek, J., Zahradník, J., & Clinton, J.: Bayesian ISOLA: New tool for automated centroid
346 moment tensor inversion, GEOPHYS J INT, 210(2), 693–705, https://doi.org/10.1093/gji/ggx158, 2017.

347 Walsh, D., Arnold, R. and Townend, J.: A Bayesian approach to determining and parametrizing earthquake focal
348 mechanisms, GEOPHYS J INT, 176(1), 235-255, https://doi.org/10.1111/j.1365-246X.2008.03979.x, 2009.

349 Wéber, Z.: Probabilistic local waveform inversion for moment tensor and hypocentral location, GEOPHYS J INT,
350 165, 607–621, https://doi.org/10.1111/j.1365-246X.2006.02934.x, 2006.

351 Wéber, Z.: Estimating source time function and moment tensor from moment tensor rate functions by constrained L1
352 norm minimization, GEOPHYS J INT, 178, 889–900, https://doi.org/10.1111/j.1365-246X.2009.04202.x, 2009.

353 Wéber, Z.: Probabilistic joint inversion of waveforms and polarity data for double-couple focal mechanisms of local
354 earthquakes, GEOPHYS J INT, 213(3), 1586-1598, https://doi.org/10.1093/gji/ggy096, 2018.

355 Tarantola, A.: Inverse Problem Theory, ELS. ISBN 9780444599674, 1987.

356 Zahradník, J., Sokos, E.N.: ISOLA code for multiple-point source modeling – review, in: Moment Tensor Solutions -
357 A Useful Tool for Seismotectonics, edited by: D'Amico S., Springer, Berlin, Heidelberg, Germany,
358 https://doi.org/10.1007/978-3-319-77359-9, 2019.

359
360
361
362
363
364
365
366
367
368
369
370
371
372
373

374

375 **Table 1: Results of the synthetic tests with different SNR using all stations. The plots are equal-area Lambert-Schmidt**
376 **projections, lower hemisphere with compressional and dilatational polarities, in black and white respectively. The**
377 **Compressional quadrants are shaded. The input focal mechanism nodal lines are in green and the solutions' nodal lines are**
378 **in red. VR stands for variance reduction.**

Data	SNR	Strike (º)	Dip (º)	Rake (º)	DC%	CLVD%	VR	Kagan angle (º)	DC plot	Deviatoric plot
All stations With polarities and DC% > 70	No noise	87/179	75/83	173/15	76	19	0.99	4		
	1.0	84/177	67/82	171/23	85	10	0.60	8		
	0.5	82/177	65/81	170/26	79	8	0.25	10		
	0.1	332/112	60/37	-67/-124	87	12	0.005	63		

379
380
381
382
383
384
385
386
387
388
389
390
391
392
393
394
395
396

397

398 **Table 2: Mechanisms obtained using different SNR applied to the synthetic data. Only two stations (LIENZ and SGT04)**
399 **are used in the inversion. The source is fixed to the one obtained in all stations computation.**

Data	SNR	Strike (º)	Dip (º)	Rake (º)	DC%	CLVD%	VR	Kagan angle (º)	DC plot	Deviatoric plot
LIENZ + SGT04 With polarities and DC% > 70	No noise	86/179	69/84	173/21	73	3	0.99	5		
	1.0	81/176	71/77	167/19	86	14	0.58	8		
	0.5	81/176	71/77	167/19	86	14	0.24	8		
	0.1	322/151	57/33	-95/-83	73	12	0.008	85		

400

401

402 **Table 3: Results of the same inversion as in Table 2, but no polarity or DC% constraints are employed. The source is fixed**
403 **to the one obtained in all stations computation.**

Data	SNR	Strike (º)	Dip (º)	Rake (º)	DC%	CLVD%	VR	Kagan angle (º)	DC plot	Deviatoric plot
LIENZ + SGT04 Without polarities and free DC%	No noise	87/180	72/80	170/18	89	4	0.99	2		
	1.0	79/180	63/70	157/29	72	6	0.59	17		
	0.5	66/175	55/65	149/40	49	9	0.27	30		
	0.1	39/152	56/59	142/40	48	1	0.03	48		

404

405 **Table 4: Moment tensor solutions using different data sets employing full C_D for Sargans earthquake. The first row is the**
406 **reference solution of Fig. 9 resulting from the inversion of all stations with polarity and DC% constraints. Two-station**
407 **solutions are close to the reference one in terms of deviatoric mechanism. Two datasets of LIENZ + SGT04 and SGT04 +**
408 **PANIX show identical DC solution to the reference result. That is while the one-station dataset mechanisms are often badly**
409 **estimated.**

	Data	Strike (°)	Dip (°)	Rake (°)	DC%	CLVD%	M_w	VR	Kagan angle (°)	DC plot	Deviatoric plot
With polarities and DC% > 70	Reference (Fig. 9)	88/180	80/80	170/10	72	13	3.7	0.82	4		
	LIENZ + SGT04	80/178	63/74	163/28	71	25	3.6	0.80	19		
	SGT04 + PANIX	272/180	83/71	-161/-8	77	21	3.6	0.83	20		
	LIENZ	272/181	87/80	-170/-3	78	-21	3.6	0.82	14		
	SGT04	80/178	63/74	163/28	71	25	3.6	0.79	19		
Without polarities and free DC%	LIENZ + SGT04	92/184	81/77	166/10	21	39	3.8	0.83	6		
	SGT04 + PANIX	84/182	70/70	159/21	41	26	3.7	0.86	15		
	LIENZ	12/104	83/76	166/7	42	-16	3.7	0.84	75		
	SGT04	82/184	66/64	151/27	28	39	3.6	0.84	23		

410
411
412
413
414
415

416 Table 5: Moment tensor solutions using different datasets employing full C$_D$ for Malard earthquake. The first row is the
417 solution considered as reference (red) shown also in Fig. 13 resulted from the inversion of five stations with polarity and
418 DC% constraints. The green nodal lines in the rows other than the first row are the reference solution.

	Data	Strike (º)	Dip (º)	Rake (º)	DC%	CLVD%	M$_w$	VR	Kagan angle (º)	DC plot	Deviatoric plot
With polarities and DC% > 70	Reference Fig. 13	26/119	58/84	-7/-148	87	9	3.6	0.79	3		
	HSB + VRN	26/122	65/78	-14/-154	86	3	3.7	0.79	10		
	VRN + JIR1	20/112	60/87	-3/-150	79	3	3.7	0.46	8		
	HSB	26/122	65/78	-14/-154	86	3	3.7	0.79	10		
	VRN	22/289	79/79	12/168	76	14	3.6	0.26	29		
Without polarities and free DC%	HSB + VRN	28/123	74/73	162/17	79	16	3.7	0.80	90		
	VRN + JIR1	25/293	46/88	-177/-44	70	11	3.7	0.47	91		
	HSB	28/122	74/73	162/17	79	16	3.7	0.80	90		
	VRN	141/324	61/29	89/93	10	88	3.7	0.46	95		

419

420

421
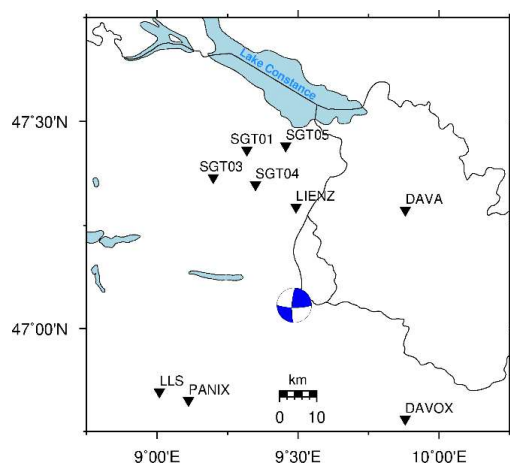
Figure 1: Map related to M_w 3.6 Sargans, Switzerland earthquake, near Liechtenstein border, applied in the synthetic tests and as the method application in the following sections. The independent beachball solution (retrieved using all stations by Bayesian ISOLA (Vackář et al., 2017)) are inserted at the epicenter and the triangles indicate the station locations. Black lines show countries' borders and lake shores.

426

427

428

429
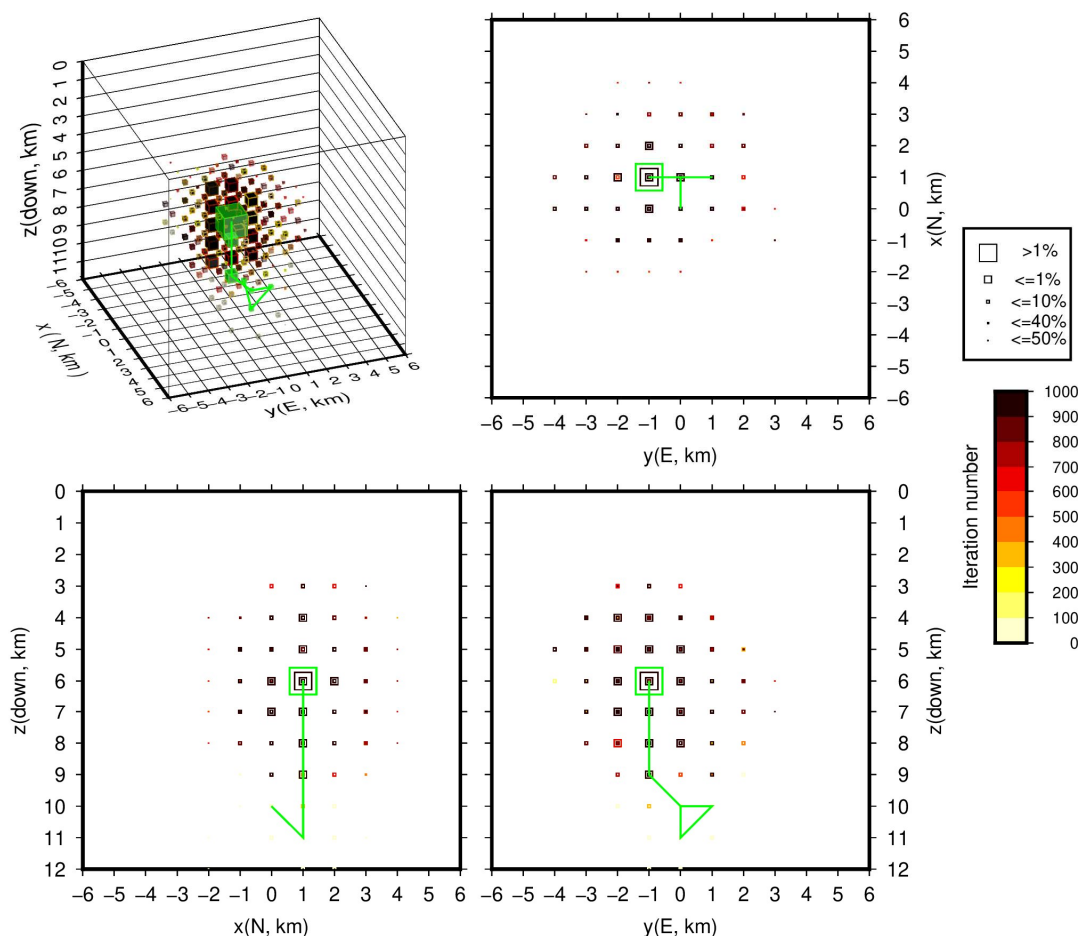
430   **Figure 2: 1000 random walks to reach the maximum a posteriori location in three and two dimensional views for the**
431   **synthetic test using all stations without noise. After 38 iterations, the walker reaches the optimum point. Cubes and squares**
432   **show proposed locations colored according to their iteration number and sized in keeping with the likelihood value, that is,**
433   **largest cubes and squares indicate greater than 1% maximum a posteriori location, etc. The green cubes in 3D view show**
434   **the accepted movements of the walker in location space with the increasing likelihoods, with their last optimum one**
435   **encircled by green squares in 2D views. There are seven accepted solutions with the increasing likelihood that their paths**
436   **are shown by green lines, reaching to the input location.**
437

438

439

440

441

442

443

444

445

446
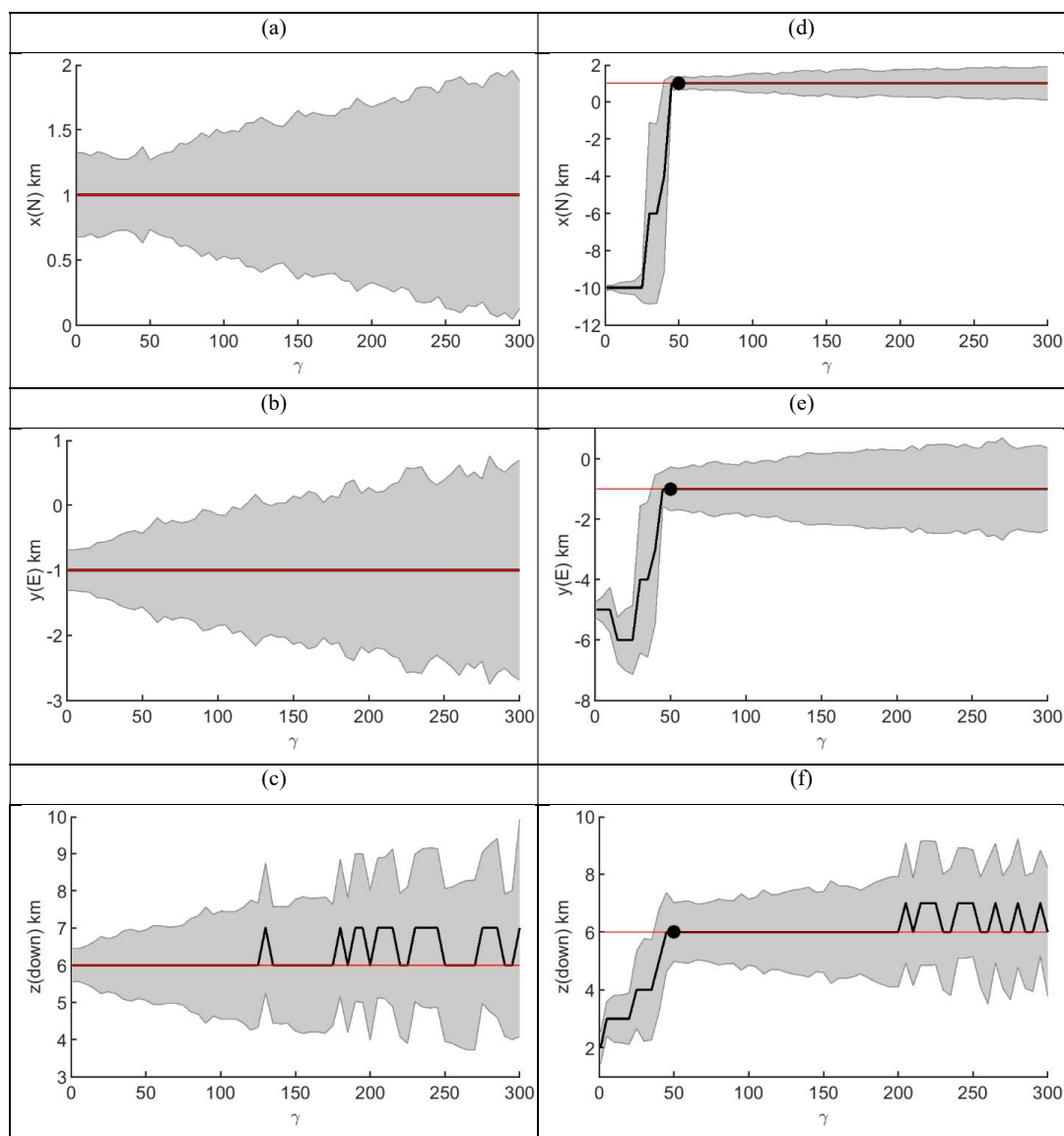
Figure 3: Source location and shaded error bars versus γ for SNR equal to 2.0 in the frequency range 0.02 - 0.15 Hz for the synthetic test. The source locations' ranges are the mean of MCMC traces. The standard deviations are in gray, the red line illustrate the correct input location. The source location in the left panel (a to c) belong to the calculations with the starting point x = (0 km N, 0 km E, 10 km down) near to the input location in the synthetic test while the right panel (d to f) shows the source locations for the farthest starting point, that is x = (-10., -10, 1). The circle show the selected γ = 50 for this test.
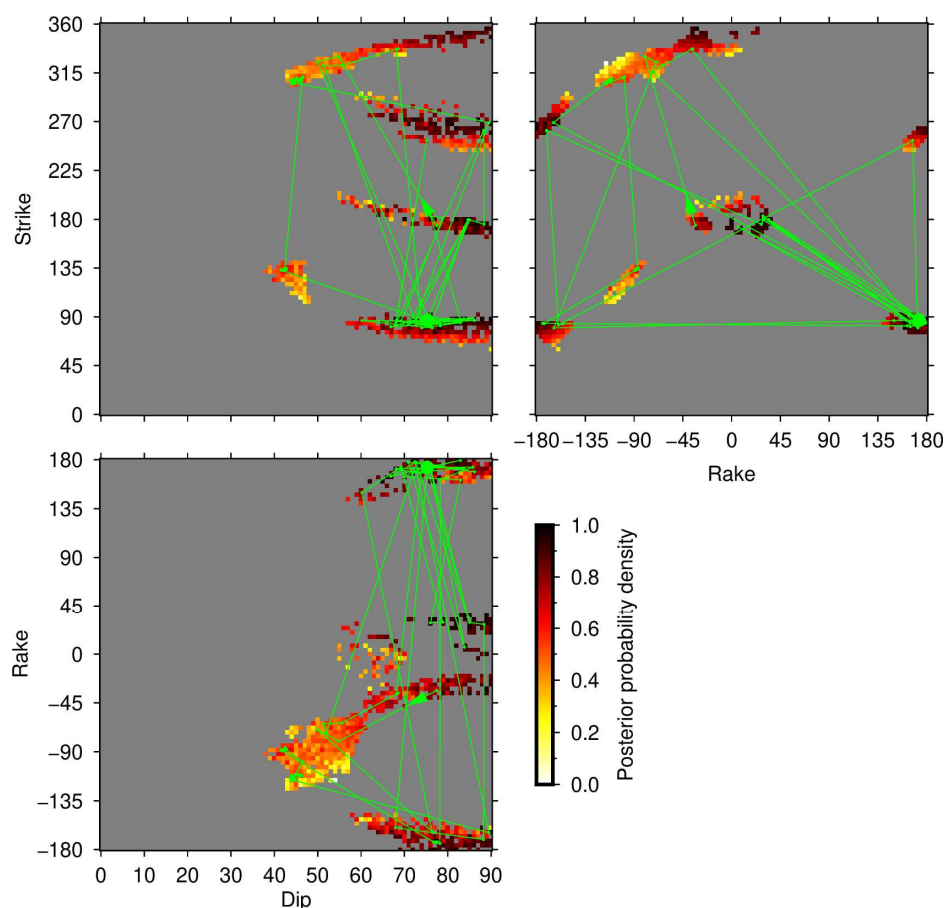
Figure 4: 2174 polarity and DC% tested focal angles out of 10^5 ones in the inner Markov chain shown by squares, colored according to the values of posterior probability density obtained applying all stations polarities and waveforms observed for the synthetic test with no noise. The steps belong to all six accepted source locations with the increasing likelihood in the outer location chain. The green lines demonstrate the accepted random walks. The green arrows represent the first point passing through the condition of larger likelihood; small green circles are subsequent points and finally the large green circles show the location of the optimum (maximum likelihood) focal mechanism (in total 87 sites for all accepted sources).
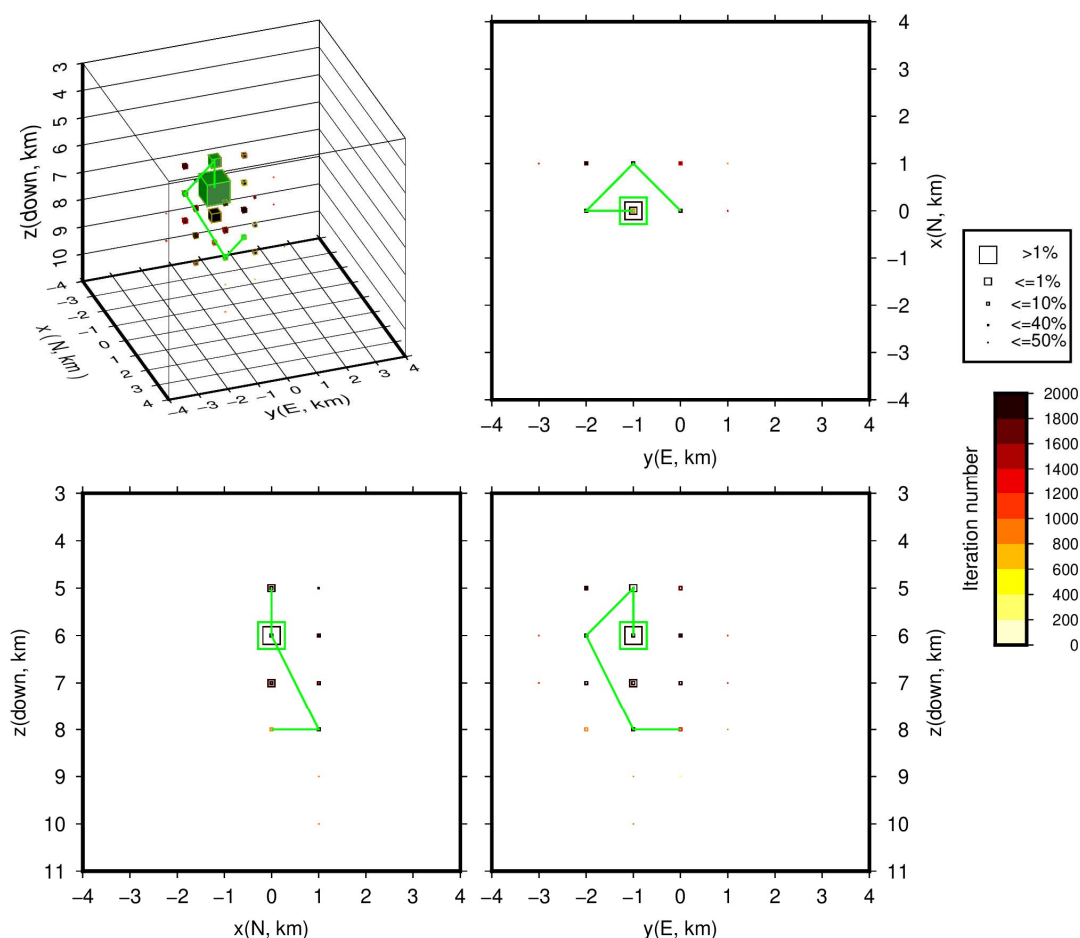
Figure 5: 409 accepted random walks to reach the maximum a posteriori location in three and two dimensional views for the inversion of Sargans earthquake data using all stations with full C$_D$ covariance matrix. 37 out of 2000 iterations are enough to find the maximum a posteriori location. The center of the Cartesian coordinate is 47.057°N and 9.486°E. There are five accepted solutions with the increasing likelihood that their paths are shown by green lines reaching to the optimum point. For the explanations of the symbols refer to Fig. 2.

478
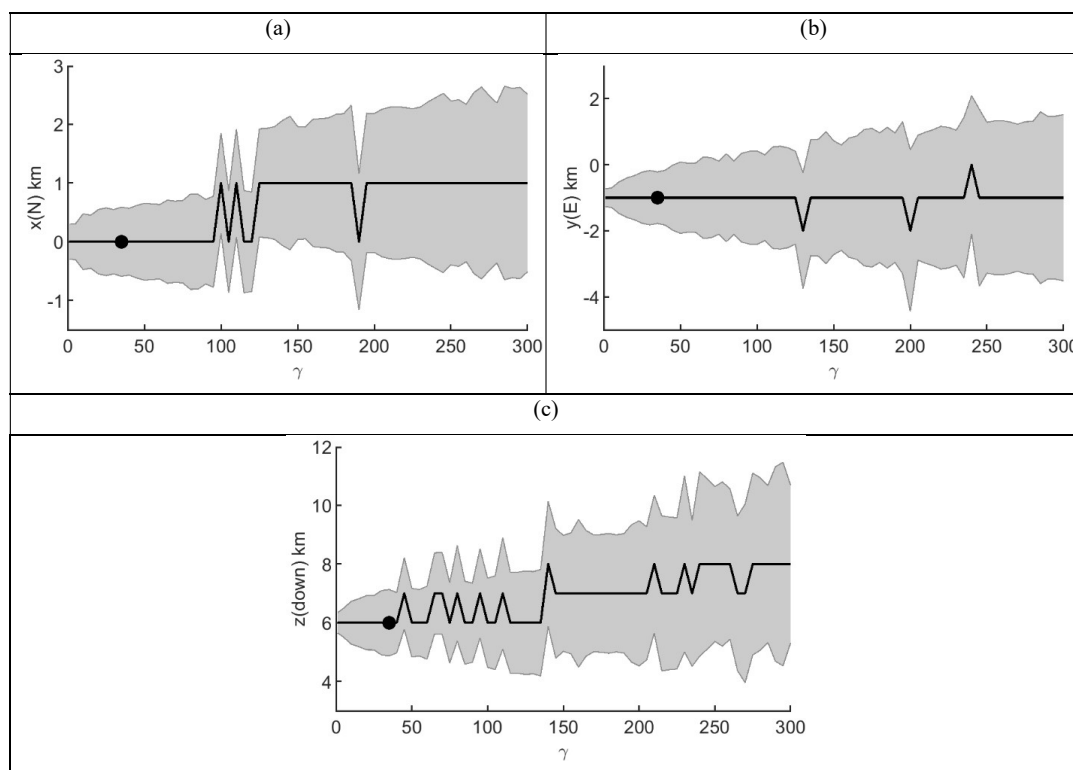
Figure 6: Source location ranges and standard deviations versus γ for Sargans earthquake. The source locations are the mean of MCMC trace shown in black line for each γ and the shaded error bars are in gray. The circle shows the selected γ.

479
480
481
482

483

484

485
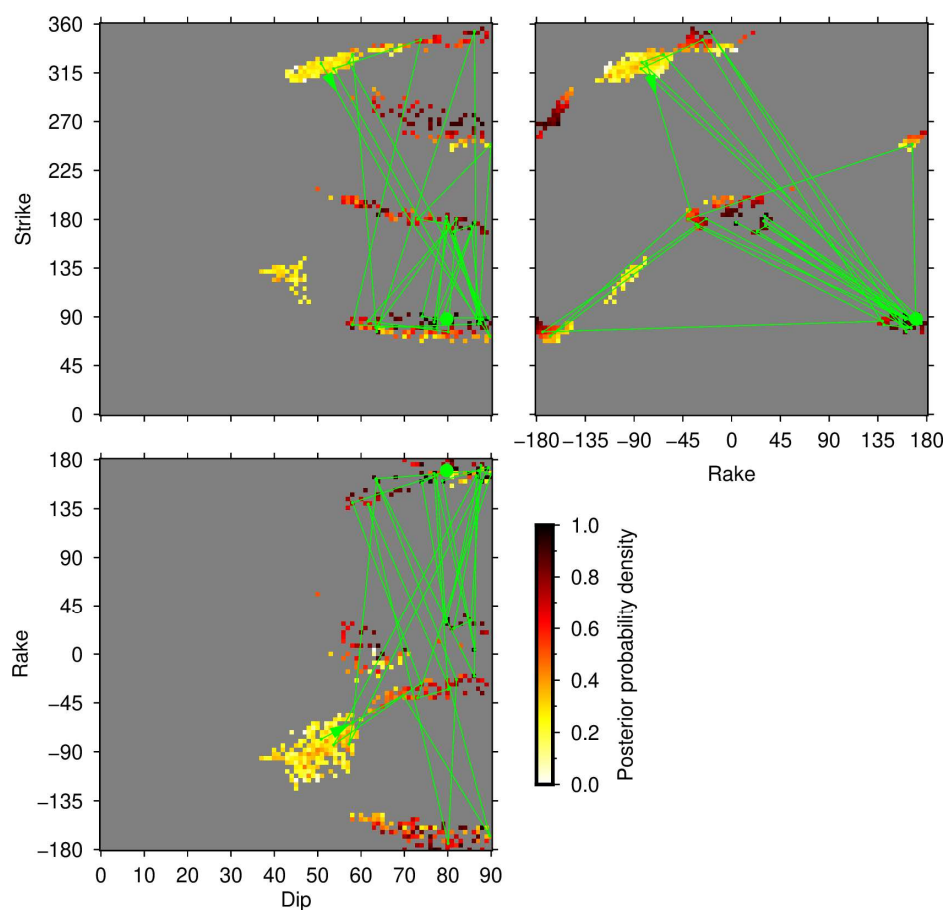
Figure 7: 638 visited sites on 2D square lattices of focal angles' space, searching for maximum likelihood point of the PPD which obtained using all stations polarities and waveforms observed and for a Sargans earthquake. The steps belong to all five accepted source locations in the outer chain. The data and theoretical errors are used in the inversion in the form of full C_D. There are in total 34 sites for all accepted sources. 1000 location sites and 10^5 MT values are polarity and DC% tested before CPU intensive synthetic seismograms calculations, leading to only 638 visited sites. For the symbols see Fig. 4.
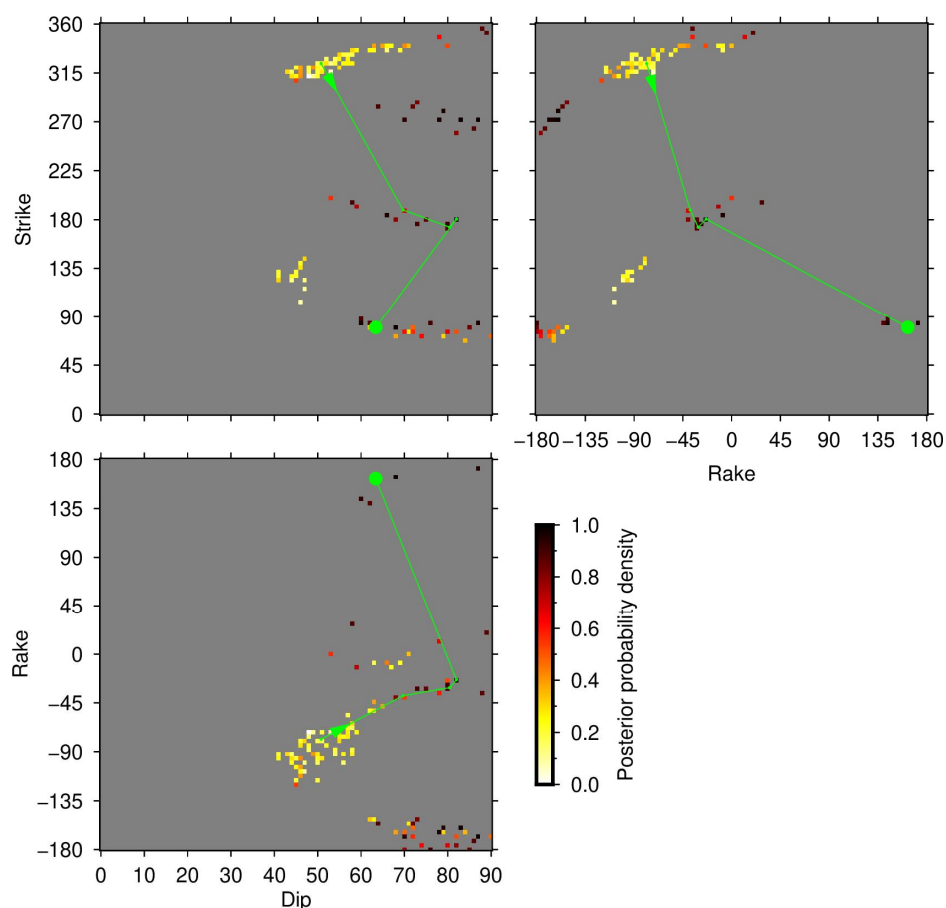
Figure 8: **Random walk of 122 trial steps on 2D square lattices of focal angles' space, searching for maximum likelihood point of the posterior probability density (PPD) which obtained using all stations polarities and waveforms observed at two stations, LIENZ and SGT04, for a Sargans earthquake. The location is fixed to the one estimated from all-station calculation. The data and theoretical errors are used through the inversion in the form of full C_D. There are in total five sites with the increasing likelihood values. The location site is fixed to x = (0.5 km N, -1 km E,   6 km down) and 10^5 MT sites are polarity and DC% tested before CPU intensive synthetic seismograms calculations, leading to only 122 visited sites. For the symbols see Fig. 4.**

(a) DC part   (b) Deviatoric part

510
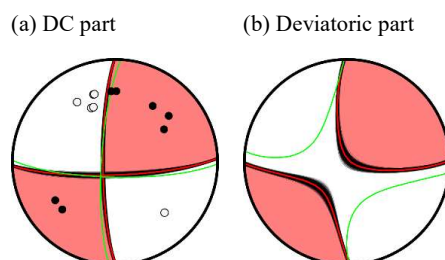
Figure 9: Moment tensor solution in case of using all stations and polarities in the inversion. The inversion is performed in the displacement domain applying full covariance matrix of both data and Green functions uncertainties. The solution is shown by red nodal line; the errors are in black and the independent solution of Bayesian ISOLA (Vackář, et al., 2017) is in green. (a) DC focal mechanism solution. (b) Deviatoric part.

515

516

517
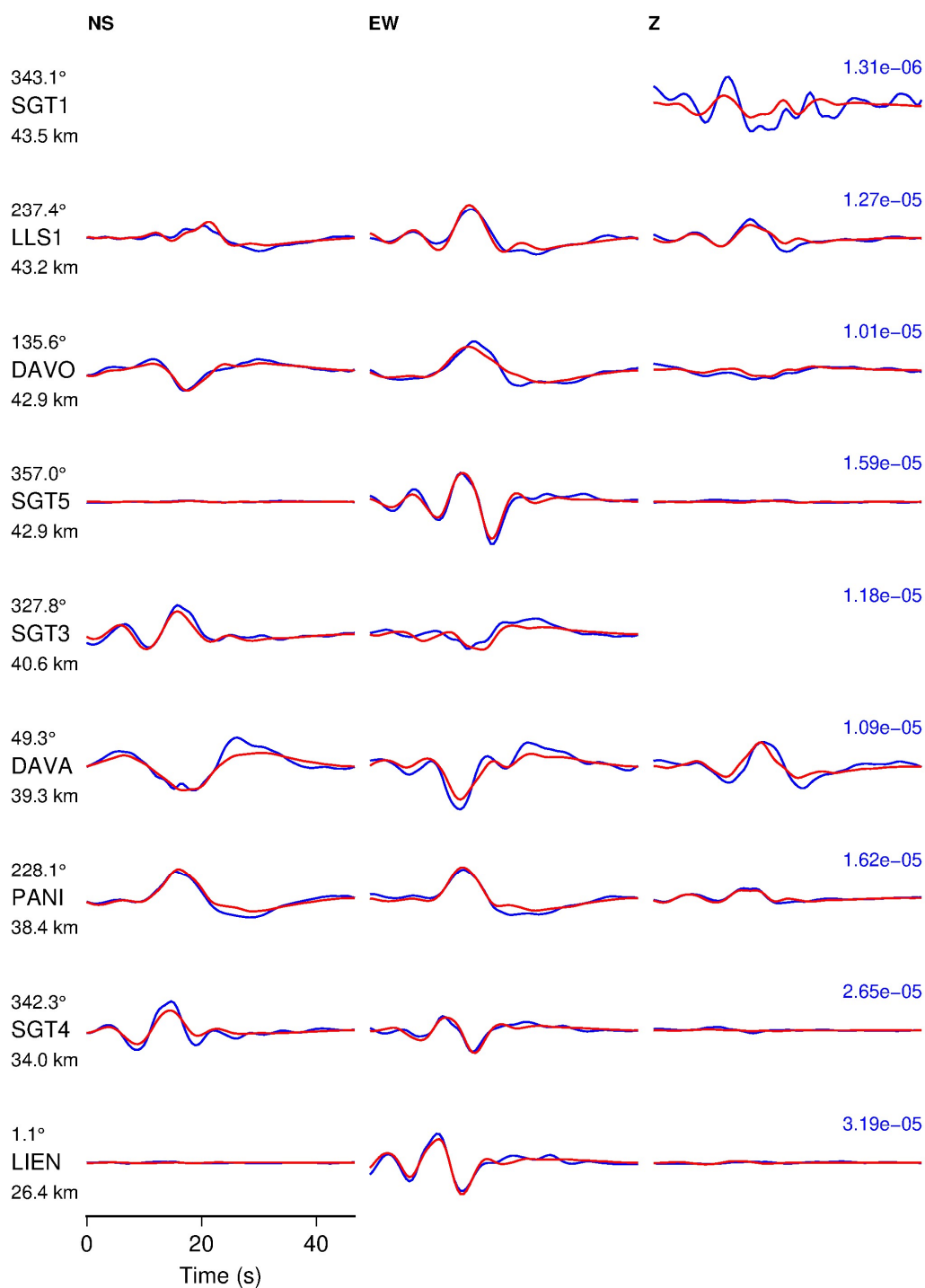
518 **Figure 10: Comparison of standardized observed (blue) and synthetic (red) displacement seismograms using all stations**
519 **and polarities in the inversion involving data and Green functions uncertainties. The waveforms are normalized by means**
520 **of the largest component of each station; that is, the largest component of each station is 1 and the numbers on the right are**
521 **the maximum amplitudes in m. The station codes, epicentral distances and azimuths are shown on the left. The variance**
522 **reduction using all seismograms is 0.82.**
523

524

525

526

527

528

529

530

531

532

533

534

535

536

537

538

539

540

541

542

543

544

545

546

547

548

549

550

551

552
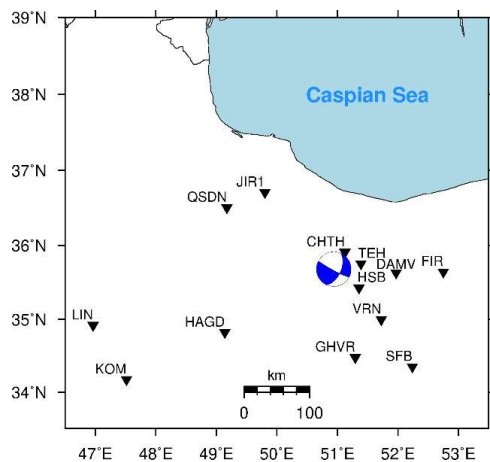
Figure 11: Map related to M$_w$ 3.8 Malard earthquake near Tehran, Iran, used as the method application. The independent beachball solution (retrieved using all stations by ISOLA) are inserted at the epicenter and the triangles show the station locations. Black lines show countries' borders and lake shores.

556

557

558
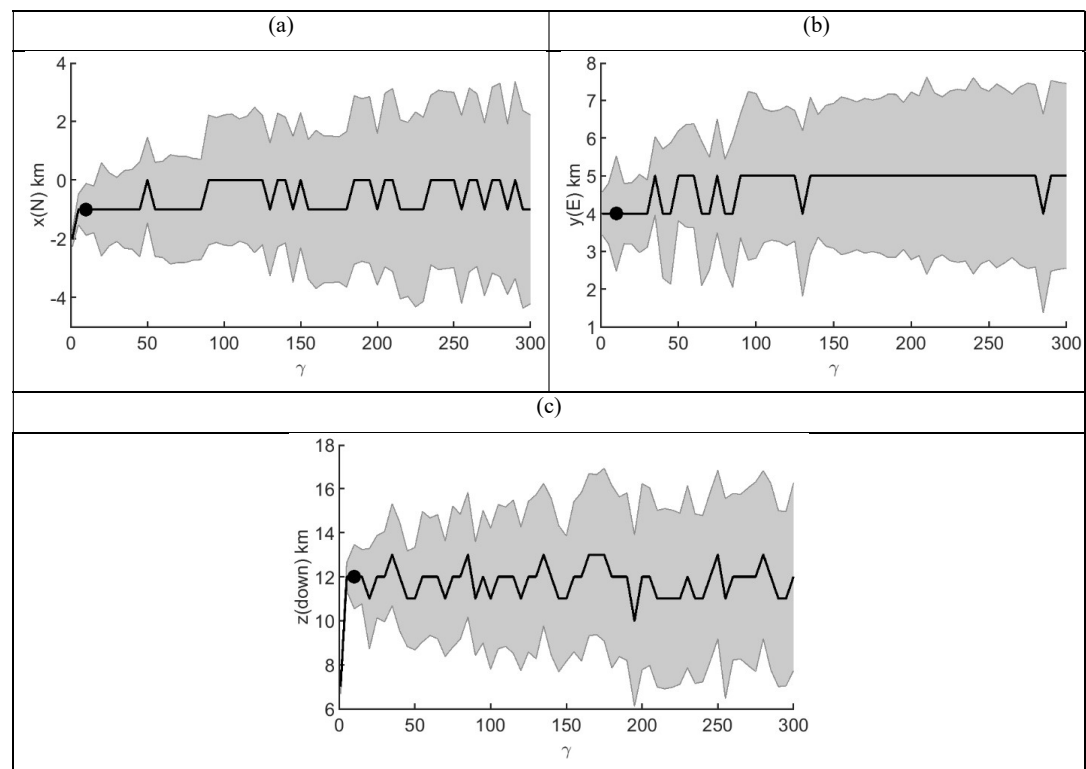
559 **Figure 12: Source location range for different γs calculated by Malard earthquake data. The filled circle illustrates the**
560 **selected γ value for computing optimum source location.**

561
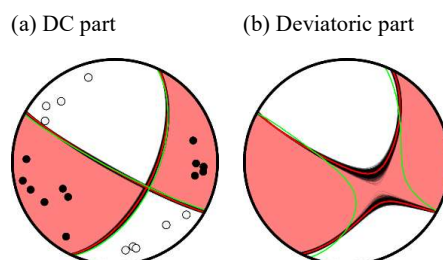
Figure 13: Focal mechanism solution of Malard earthquake obtained by five-station broadband waveform inversion with full C$_D$, constrained by first-motion polarities and DC% > 70 (red). The independent ISOLA solution obtained by 13 stations are illustrated in green and the errors are in black. a) DC part with polarities. b) Deviatoric part.

565

566

567
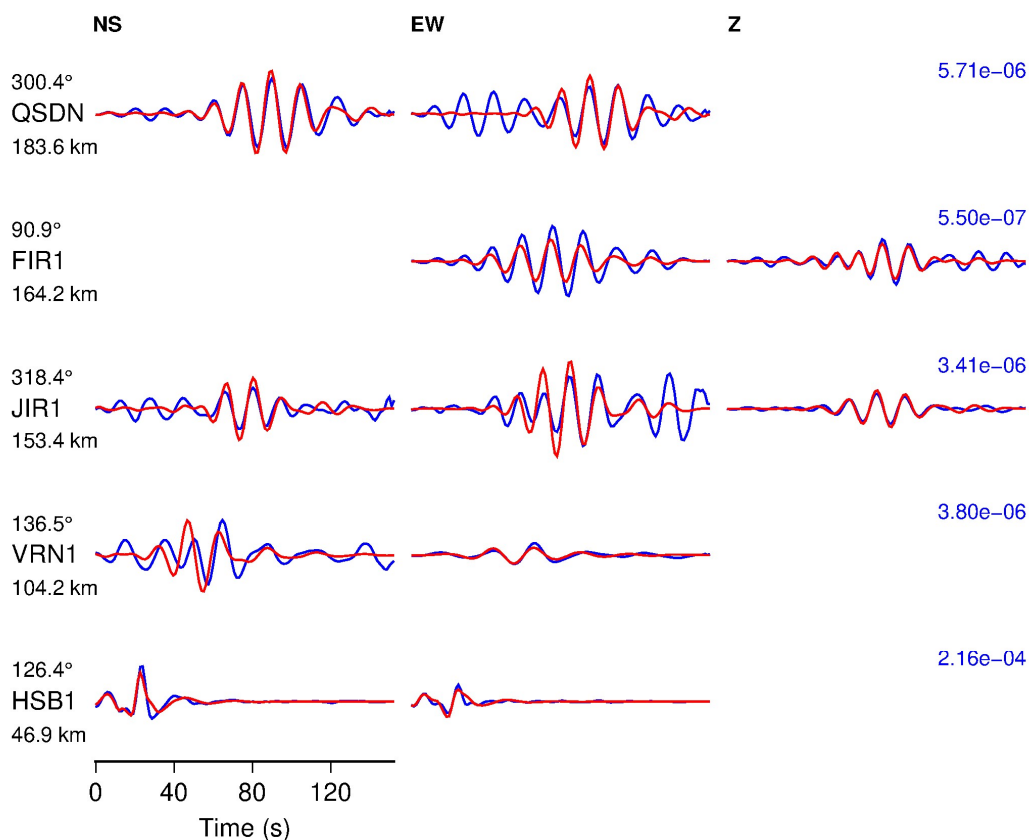
Figure 14: Observed (blue) and synthetic (red) standardized displacements for Malard earthquake. Some components are not taken into account due to unavailability. For details refer to Fig. 10.